Mapping Pulsatile Optic Nerve Head Deformation using OCT

Marissé Masís Solano, MD,[1,2] Emmanuelle Richer,[1,3] Farida Cheriet, PhD,[3] Mark R. Lesk, MD,[1,2] Santiago Costantino, PhD[1,2]

Objective: To develop a noninvasive technique to quantitatively assess the pulsatile deformation due to cardiac contractions of the optic nerve head (ONH).

Design: Evaluation of a diagnostic test or technology.

Participants: Healthy subjects with no history of refractive surgery, divided into 2 cohorts on the basis of their axial length (AL).

Methods: We present a noninvasive technique to quantitatively assess the pulsatile deformation of the ONH tissue by combining high-frequency OCT imaging and widely available image processing algorithms. We performed a thorough validation of the approach, numerically and experimentally, evaluating the sensitivity of the method to artificially induced deformation and its robustness to different noise levels. We performed deformation measurements in cohorts of healthy (n = 9) and myopic (n = 5) subjects in different physiological strain conditions by calculating the amplitude of tissue displacement in both the primary position and abduction. The head rotation was measured using a goniometer. During imaging in abduction, the head was rotated $40° \pm 3°$, and subjects were instructed to direct their gaze toward the OCT visual target.

Main Outcome Measures: Pulsatile tissue displacement maps.

Results: The robustness of the method was assessed using artificial deformations and increasing noise levels. The results show acceptable absolute errors before the noise simulations grossly exaggerate image degradation. For the group of subjects with AL of < 25 mm (n = 9), the median pulsatile displacement of the ONH was 7.8 ± 1.3 μm in the primary position and 8.9 ± 1.2 μm in abduction. The Wilcoxon test showed a significant difference ($P \leq 0.005$) between the 2 paired measures. Reproducibility was tested in 2 different sessions in 5 different subjects with the same intraocular pressure, and an intraclass correlation coefficient of 0.99 was obtained ($P < 0.005$).

Conclusions: The computational pipeline demonstrated good reproducibility and had the capacity to accurately map the pulsatile deformation of the optic nerve. In a clinical setting, we detected physiological changes in normal subjects supporting its translation potential as a novel biomarker for the diagnosis and progression of optic nerve diseases. *Ophthalmology Science* 2022;2:100205 © 2022 by the American Academy of Ophthalmology. This is an open access article under the CC BY-NC-ND license (http://creativecommons.org/licenses/by-nc-nd/4.0/).

Supplemental material available at www.ophthalmologyscience.org.

Ocular biomechanics are progressively taking a bigger role in clinical care and research in ophthalmology. Specifically for the cornea, the biomechanical characteristics of the tissue are currently part of routine clinical assessment. However, for the optic nerve head (ONH), which plays a major role in glaucoma, a noninvasive and reliable test to apply in everyday practice has yet to be developed.

Early studies on ONH biomechanics focus on the response to intraocular pressure (IOP) changes.[1] Different techniques have been described such as x-ray photography of cadaveric nonhuman primate eyes with fine platinum wires inserted into the peripapillary sclera and optic disc,[2] laser Doppler velocimetry of normal human autopsy eyes,[3] conventional histology of human eyes,[4] and image-based biomechanical analysis.

Improved light sources and scanning methods in OCT have led to high-resolution imaging, fast enough to record the movement and deformation of tissue.[5] Swept-source OCT provides deep imaging capability and has been used in vivo to assess the architecture and biomechanical characteristics of the lamina cribrosa (LC) in the human eye using static images.[6,7] The cardiac cycle drives pulsatile deformations of the ONH that are caused by blood flow into the retinal and choroidal vasculature and the resultant pulsatile IOP changes,[8] providing an opportunity to probe the tissue's physiological changes as has been done in other medical disciplines.[9,10] However, most available research has focused exclusively on static LC properties such as depth, anterior lamina insertion, and local thickness.[7] This gap presents novel opportunities for

glaucoma research, and the clinical assessment of biomechanics of the tissue as a risk factor in the development of the disease[11] is becoming feasible.

Recent studies have focused on the quantification of movement using OCT,[12−14] introducing the concept of pulsation to image processing in ophthalmology. Specifically for the ONH, the pulsatile dynamics have been used to analyze blood flow,[8,15] yet the effect of pulsations on the surrounding tissue has not been thoroughly described. Recent studies in rodents[16] and nonhuman primates[17] have exploited video OCT to probe the biomechanics of the ONH; however, to date, this has not been achieved in human subjects. Indeed, human in vivo characterization of pulse-induced ONH deformation could provide valuable information for evaluating the biomechanical properties of the glaucomatous optic nerve. Moreover, because it has the advantage of being noninvasive and of only using ubiquitous technology already available in most eye clinics, it could easily translate to the clinical setting and become a useful tool to improve care.

Methods

Study Participants and Imaging

Study Participants. This study was approved by the institutional review board of the Maisonneuve-Rosemont Hospital and performed in accordance with the 1964 Declaration of Helsinki and its amendments. Written informed consent was obtained from all participants.

Subjects with no ocular pathology besides myopia and age > 18 years were included in the study. The same trained ophthalmologist (M.M.S.) performed OCT imaging and a complete ophthalmic examination (visual acuity, IOP, slit lamp examination, eye fundus evaluation, refraction, and axial length [AL] measurement). If the subject was eligible, the individual (M.M.S.) performed the OCT imaging.

All subjects included in the study underwent, in addition to the clinical examination, the same OCT imaging, heart rate measurement (Digital pulsimeter OxiMax N-65), IOP measurement (Pascal DTC tonometer), and AL evaluation (Zeiss IOL master 500).

Data obtained from these participants have not been used in any of the previously published work.

Imaging. We used a swept-source OCT (PlexElite 9000) with customized settings to acquire videos at an A-scan rate of 100 kHz, which allowed us to obtain consecutive B-scans of 6 mm over the same area (with a B-scan rate of approximately 100 Hz). The resolution of the OCT machine is 6.3 μm axially and 20 μm transversally. Movies of 3000 B-scans were obtained per subject, with an approximate video length of 30 seconds and an image size of 1536 × 1024 pixels per B-scan. Pixel size was 1.95 μm in the vertical direction and generally 5.9 μm in the horizontal direction. Ocular magnification changes caused by differences in ALs were corrected.

Images were acquired with no pupillary dilation under dim light conditions. Subjects with difficulty to fixate or media opacities were not included in the study; the included subjects were not dilated by the time of the examination because it would not have improved the acquisition.

The head rotation was measured using a goniometer. During imaging in abduction, the head was rotated 40° ± 3°, and subjects were instructed to direct their gaze toward the OCT visual target.

Eye tracker. Our OCT machine is equipped with an eye tracker, which constantly monitors the ocular fundus to guarantee that the same region of the eye is scanned throughout the recording. When patients blink or shift their gaze, the acquisition is automatically paused and only resumes once the same area can be properly scanned again. Displacement fields comparing frames with an intervening eye tracker pause are never considered in the analysis, as these fields may be due to suboptimal repositioning of the laser beam.

Statistics. R programming software (R software, version 1.2.5033) was used to perform the statistical analysis. Descriptive statistics were applied to demographic data (mean age, sex, and IOP). Student *t* test, Wilcoxon test (in nonparametric distribution data), and analysis of variance were used for continuous and categorical variables. Multivariate analysis was performed to determine the correlation between pulsatile optic nerve deformation, demographic data, and clinical data (age, IOP, and AL). A test−retest validation was used to evaluate the intraclass correlation coefficient for the algorithm reproducibility.

Analysis Pipeline

We mapped ONH tissue deformation caused by the pulsatile changes in the blood flow by combining advances in imaging technology and image processing. We used a swept-source OCT to acquire high-frequency videos. The analysis of deformation is based on a rigid registration of all frames of the movie, followed by a nonrigid registration using the demons algorithm[18−22] to measure the displacement fields between pairs of frames (Fig 1). The final deformation map is created by averaging such displacement fields throughout the movie.

Images were initially aligned in 2 steps: (1) a large median filter was applied to all images in the series, and the cross-correlation was used to perform a first rigid translation with respect to 1 arbitrary fixed frame in the movie; and (2) a second rigid registration using the original nonfiltered images was applied to adjust for rotation of the images and more fine details (Fig 1A, B). This first step of the pipeline corrects for the subject's movement during the acquisition.

Image registration was performed using the *imregister* algorithm available in MATLAB (Version R2021a). Before registration, a median filter was applied (kernel size 40 × 40), and an initial rigid translation was performed using an arbitrary chosen fixed image. A second rigid registration was then applied to correct for rotation. Once images were registered, they were assessed by the observer to corroborate quality. The images were not denoised before the registration in fear that doing so would modify the small natural movement of the tissues and, thus, influence the deformation computed.

We calculated the displacement field $\vec{u}(x, y, t)$ needed to transform 1 image into the next one, for all subsequent pairs of frames. These $\vec{u}$ vectors represent the displacements that link every pair of pixels between 2 consecutive images, that is, the nonrigid transformation that needs to be applied to 1 image to obtain a slightly modified one.[23] We computed such displacement fields for every pair of frames using a demons registration algorithm and the Mattes mutual information (MMI) metric.[18−22] We then calculated the mean absolute value of the displacement vector for every pixel along all frames of the movie (Fig 1C, D). The final result is presented as a map of time-averaged tissue displacement, where a color hue is used to indicate the magnitude of displacement (Fig 1 E, large movement is yellow/orange, small movement is green/blue).

A typical movie consists of 3000 frames, acquired approximately every 10 milliseconds, over half a minute. We can thus calculate 2999 displacement fields $\vec{u}(x, y, t)$ over consecutive
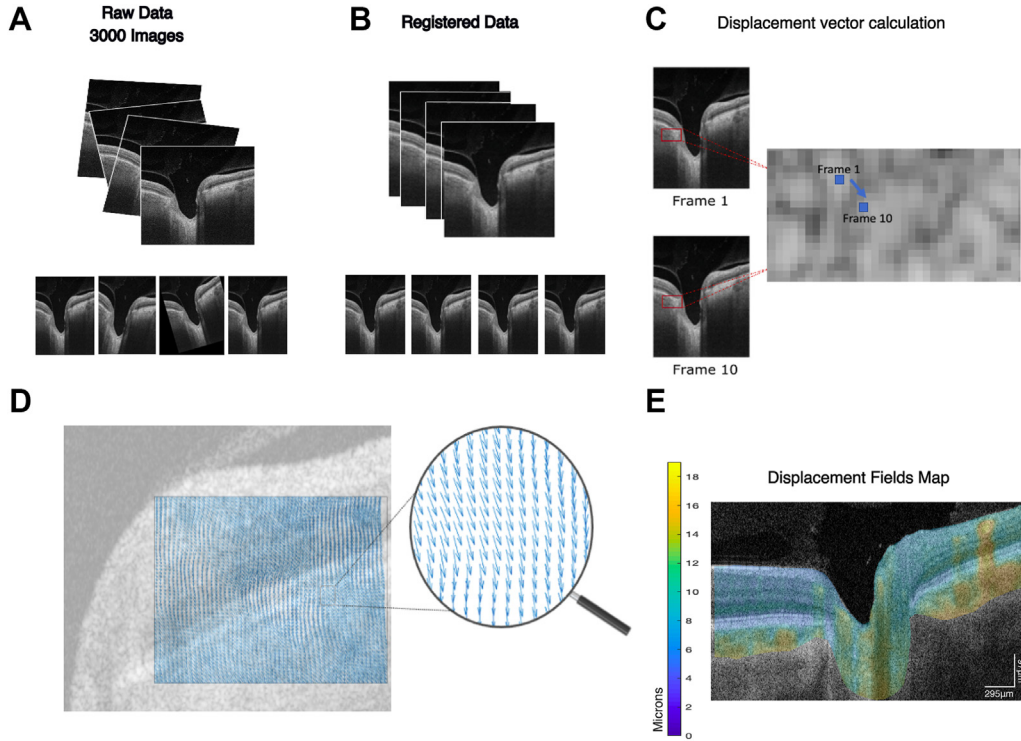
Figure 1. Pipeline to obtain the pulsatile displacement fields. **A**, Initially a 3000-frame OCT time lapse is obtained. **B**, Images are aligned by rigid registration. **C**, Demons algorithm is applied to obtain displacement fields that describe tissue changes for every pair of images. **D**, Displacement vectors are calculated for every pixel in each pair of images, and the median absolute value of this field is calculated for the entire video. **E**, Graphical representation of the local changes in the median pulsatile deformation on 1 B-scan.

frames $[I(t_i) \rightarrow I(t_{i+1})]$; however, as physiological changes are mostly because of cardiac pulsations, any 2 images obtained only 10 milliseconds apart contain almost identical information and make the computation of small $\vec{u}(x, y, t)$ very sensitive to noise. Nevertheless, the time lag $\Delta\tau$ between frames is a parameter that can be modified, and calculating $\vec{u}$ over nonconsecutive images renders larger deformations, which is achieved by increasing $\Delta\tau$ between images, thus comparing $I(t_i) \rightarrow I(t_{i+\Delta\tau})$, $I(t_{i+1}) \rightarrow I(t_{i+1+\Delta\tau})$, etc. Using a larger $\Delta\tau$, the number of displacement fields computed remains practically identical but considers larger changes between images, facilitating analysis and minimizing the effect of potential sources of noise. Thus, we can create maps of tissue displacement for different values of $\Delta\tau$, that should display the same overall behavior.

Tissue displacement was calculated separately in both axes and transformed from pixels to microns based on the axial and lateral scales provided by our machine, that is, a pixel size of 1.95 μm vertically and 5.9 μm horizontally. The small correction because of different OCT magnification as a function of AL was also considered for calculations.

Quality Control

We performed 2 control calculations for validating the analysis of a video, adequacy of frame registration, and robustness of computation of displacement fields. The quality of videos can be affected by frequent loss of tracking and movement, which is particularly common when they are obtained in abduction. The adequacy of image rigid registration was assessed using the MMI[24,25] between the frame used as a reference for the rigid registration and the subsequent registered images of the movie. A drift of MMI as a

function of time is indicative of accumulated errors in registration and could suggest a loss of tracking. Thus, only videos with a stable MMI, namely a temporal evolution of the metric with a slope of zero, were included in the study.

Additionally, we calculated 2 displacement maps for each video, 1 for $\Delta\tau = 10$ frames and 1 for $\Delta\tau = 9$ frames, and linear regression of the magnitudes on these maps, pixel-by-pixel. These 2 displacement maps correspond to $\Delta\tau$ s that only differ by 10%; thus, they must display very similar behavior. However, they were created using $\vec{u}(x, y, t)$ based on completely different pairs of images. Figure 2 shows the linear regression of deformation maps computed using $\Delta\tau$ 9 and 10 for the same video, where the similarity of both deformation maps becomes obvious. All the included videos have a linear regression slope between 0.9 and 1.045 and R^2 between 0.9989 and 0.9996. A weak correlation, or a slope far from 0.9 between $\Delta\tau$ 9 and 10, would have suggested that calculated displacement fields in 1 or both videos may be unrelated to biological deformation but may be because of noise artifacts or bad quality registration.

A total of 60 videos of 30 different subjects were acquired and analyzed, and 10 additional videos of 5 different subjects were included for the reproducibility experiment. After rigorous assessment, only videos showing a stable registration were included, to decrease the bias caused by nonbiological tissue deformation affecting the estimation made by the algorithm. Ten videos of 5 patients were used for the repeatability study ("Reproducibility" section of Results), and 28 videos of 14 patients were used for the physiological deformation experiment ("Physiological Deformation" section of Results).

The ONH area was manually traced by the same observer in all cases, using the Bruch's membrane openings as references. The
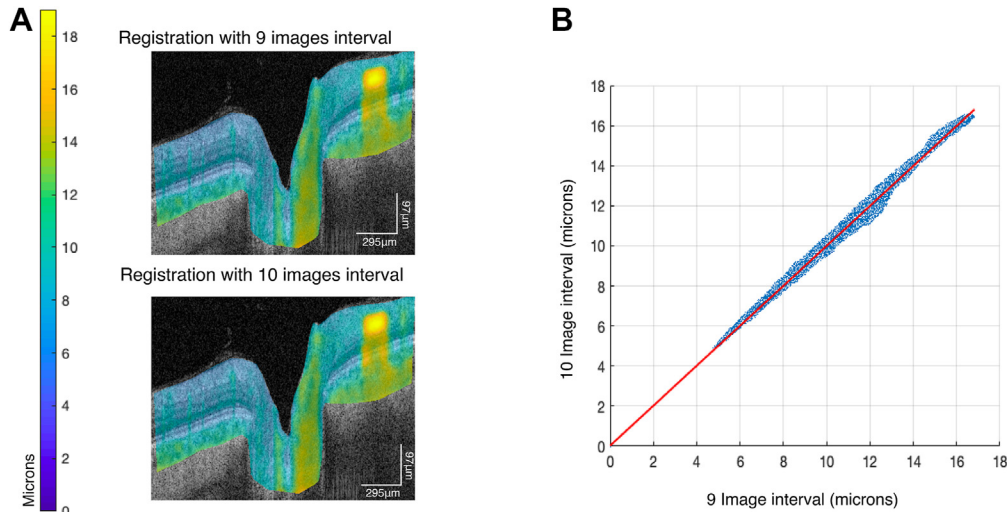
Figure 2. Two deformation maps can be calculated using different sets of image pairs for the same movie. Using $\Delta\tau = 9$ and $\Delta\tau = 10$ between images provides a self-test ro analyze the robustness, as both maps must display almost identical information. **A,** Example of 2 deformation maps using different intervals. Top image shows a displacement map using a 9-frame interval ($\Delta\tau = 9$) calculation. Bottom image shows a displacement map using a 10-frame interval ($\Delta\tau = 10$) calculation. **B,** The mean displacement calculated for different $\Delta\tau$ is compared pixel-by-pixel, and a linear fit yields a slope close to 1 and R^2 of 0.99.

included area was the tissue in between both landmarks, the vitreous interphase and the posterior border of the LC. The area between the internal limiting membrane and retinal pigment epithelium/Bruch's membrane complex was manually delimited in both nasal and temporal retinas.

Role of Vessels in Deformation Measurements

With the aim of separating pixels corresponding to vascular and retinal tissue, we traced masks, both automatically and manually. For an automated vascular segmentation, we created an ad hoc OCT angiography image[11,26,27] by computing the variance of the signal over a moving window of 6 frames throughout the time series. Such OCT angiography images were processed using a threshold to calculate a vascular mask and to restrict displacement fields to avascular zones to confirm that the changes observed between primary and abduction positions are consistent. Finally, we generated a noise-reduced video where vessels can easily be identified for manual segmentation. Such noiseless videos display only 1 cardiac period in which all frames that correspond to the same moment on the heart cycle are averaged. We used the heart rate, measured in patients at the time of imaging, to determine the phase of each frame in the movie with respect to a perfect sinusoidal function, and averaged them. The results of these methods allowed us to measure the deformation differences in areas corresponding mostly to the vascular tissue and areas without large vessels.

Results

Numerical Benchmark

Artificial Deformations. To test the dynamic range of tissue displacements that could be assessed using this pipeline, we simulated anatomical changes by deforming real OCT images. An artificial displacement field $\overrightarrow{\mu_a}$ was created to replicate the movement of natural filling of the choroid, retina, and ONH. An example of these artificial fields is

shown in Figure 3, where the displacement vectors are transformed into scalars as $\mu = \sqrt{\mu_x^2 + \mu_y^2}$ to create the heatmap shown in Figure 3A.

After manual delineation of the contours of these regions, a displacement field was created by convolving a Gaussian kernel of varying amplitude (A) and standard deviation (σ) on each pixel of these contours. The same parameters (A and σ) were used on both the y- and x-axes to simulate anterior−posterior and temporal−nasal displacements, respectively. The resulting deformation field $\overrightarrow{\mu_a}$ was then applied on several images to induce movement, after which we used the analysis pipeline to measure the displacement field $\overrightarrow{\mu_m}$. We varied A and σ to change the magnitude of the artificial deformation fields and compared them with the fields computed by the analysis pipeline. The mean and median absolute errors between both artificial $\overrightarrow{\mu_a}$ and measured $\overrightarrow{\mu_m}$ displacement fields were then computed (Fig 3B). Both the mean and median errors were only considered for pixels where the absolute value of $\overrightarrow{\mu_a}$ was > 0.1 pixel, and this workflow was repeated for 10 different images of 12 different subjects; the values shown correspond to the mean of such 120 images. This mean was calculated across all images and subjects (Figs 3, 4), as well as within each subject and subsequently across all subjects. Both ways of computing the averaged errors led to similar results. The results show that both the mean and median absolute error $|\mu_a - \mu_m|$ were < 0.12 μm in the range of physiologically realistic displacements. Only when the amplitude of the displacement was grossly exaggerated, an increase in the mean absolute error was observed (Fig 3B).

Noise Simulation. The second part of the numerical benchmark was aimed to determine the algorithm's performance under different noise scenarios added to real OCT images. Noise was created using either Gaussian or Speckle distributions of different variances and was added to the
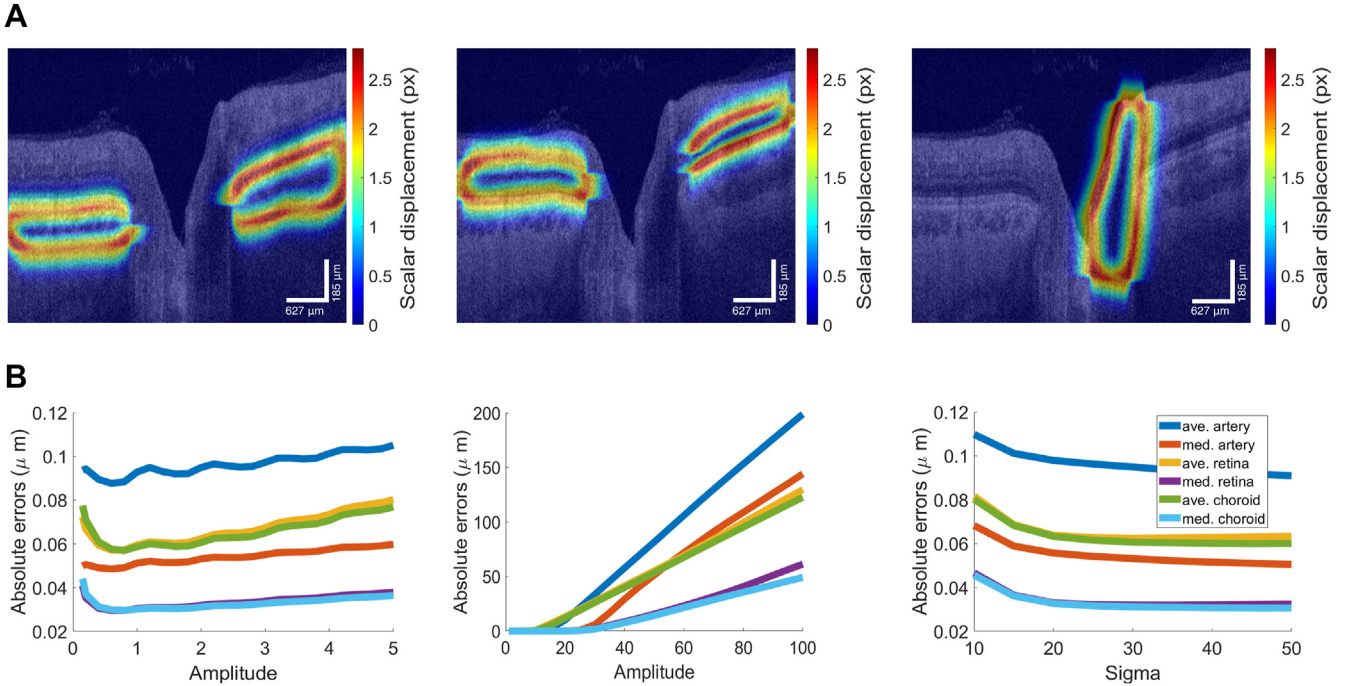
A

B

Figure 3. Simulation tests. **A**, Real B-scans were artificially deformed by a known displacement field and compared with fields obtained using the demons algorithm. Deformation fields were transformed into scalars ($\mu = \sqrt{\mu_x^2 + \mu_y^2}$) before being plotted as a heatmap. In this specific example, the amplitude and standard deviation of the Gaussian curves used in the artificial field were of, respectively, 2 and 30 pixels in the x and y directions. These artificial displacement fields were created in 3 regions of the eye—the choroid (left), retina (middle), and optic nerve head (right). **B**, Absolute errors between the applied deformation fields and computed deformation fields as a function of the amplitude (left) and standard deviation (right) applied. Absolute errors corresponding to large amplitude displacements (middle).

OCT scans (Fig 4 and Supplemental Appendix 1 [available at www.ophthalmologyscience.org]). Images were artificially deformed, and noise was added to both the original and artificially deformed images. The measured displacement field $\overrightarrow{\mu_m}$ was compared with $\overrightarrow{\mu_a}$, and the mean and median absolute errors between both deformation fields were computed. The procedure was repeated for 10 different images of each of the 12 different subjects, and the errors were averaged over all 120 images. The noise naturally found in the images was estimated. One observer segmented 5 arbitrary located regions in the retinal pigment epithelium layer of 1 OCT scan. Assuming constant values of intensity in the retinal pigment epithelium layer, the variance was computed on these regions. The variance found (0.013) was used to center the variance of the noise distributions added to the OCT images. As shown in Figure 4B and Supplemental Appendix 1, results display a decrease in the performance of the analysis method for both Gaussian and Speckle noise. For a variance of noise realistically found in our OCT images (10^{-2}), the absolute error achieved was approximately 1 μm and 1.5 μm for the Speckle and Gaussian distribution, respectively.

Clinical Validation

Reproducibility. We conducted a test−retest validation experiment on 5 different healthy individuals (mean age,

42.4 years) measured approximately 2 weeks apart. Goldmann applanation was performed to verify IOP before both sessions. We included subjects who varied by ≤ 2 mmHg between time points, based on the standard deviation of the technique.[28] Subjects with diurnal variations of > 2 mmHg were not included in the cohort to minimize the confounding effect of IOP changes on the ONH.

Maps that describe the median of the absolute value of the displacement fields as a function of time for all B-scans $M(x, y) = median(|\overrightarrow{\mu}(x, y, t)|)$ were calculated for each subject in both sessions, with $\Delta\tau = 100$ milliseconds (10 frames).

The results comparing the deformation in the ONH show an intraclass correlation coefficient of 0.99, with a *P* value of < 0.005. Figure 5A illustrates an example of 2 different maps obtained on the same subject at 2 different time points. Figure 5B describes the mean pulsatile deformation correlation for all subjects in different anatomical zones (nasal retina, temporal retina, and ONH) at different time points at the same IOP levels.

Frequency Analysis. We verified that tissue deformation is driven by cardiac pulsation and blood flow using frequency analysis. We used the temporal evolution of the displacement fields to recreate the movement of the tissue. We chose arbitrary locations in the first image that determined the position of a tissue section represented by the pixel x_1, y_1, t_1 and, using the displacement field at that location $\mu(x_1, y_1, t_1 + \Delta\tau)$, we obtained its position in the
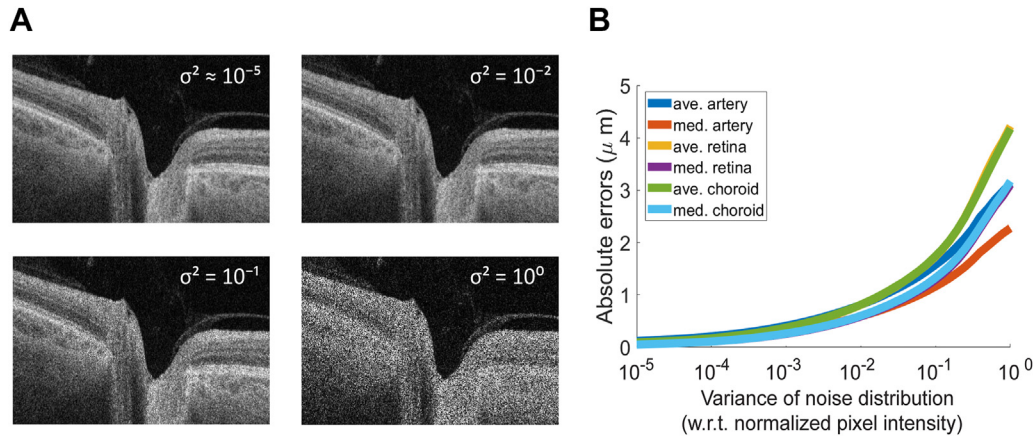
Figure 4. Gaussian and speckle noise distributions were applied to test the accuracy of the algorithm. **A,** Examples of added Speckle noise of different variance applied to real B-scans. **B,** Mean and median absolute error of the calculated displacement fields as a function of noise amplitude (Speckle distribution). The values of variance added are between 0 and 1 and refer to normalized values of pixel intensity.

following frame $x_2, y_2, t_1 + \Delta\tau$. Thus, the same tissue section in the third $x_3, y_3, t_1 + 2\Delta\tau$ frame is given by $\mu(x_1, y_1, t_1 + 2\Delta\tau)$. An example of these trajectories is presented in Figure 6, where the movement in both directions, anterior−posterior and nasal−temporal, can be observed. Because the data are not equidistant in time (because of eye tracker pauses), Lombe−Scargle periodograms were computed. Peaks in the frequency space near 1.3 Hz indicate that cardiac pulsations are the main driver of the deformations that we measure, which corresponds to the heart rate of the subject in this example (measured with a pulse oximeter).[29,30]

Physiological Deformation. Based on previous studies, it has been shown that eye rotation yields significant strain on the ONH and peripapillary tissues.[31−35] Based on this concept, we applied changes in eye gaze as a means of inducing added physiological tension on the ONH tissue. Imaging was performed in the primary and abduction positions; because of the OCT apparatus design, it was not possible to obtain good-quality images in adduction. A total of 14 subjects were imaged in 1 eye, in both positions.

Recruited subjects were 54.6% women, with a mean age of 41 ± 12 years and a mean IOP of 17 ± 1.5 mmHg. No significant differences were found between the AL of < 25 mm (n = 9) and the AL of $\geq$ 25 mm (n = 5) groups.

Figure 7A illustrates a representation of 2 different displacement maps in the primary position and abduction corresponding to the same subject. Maps of median
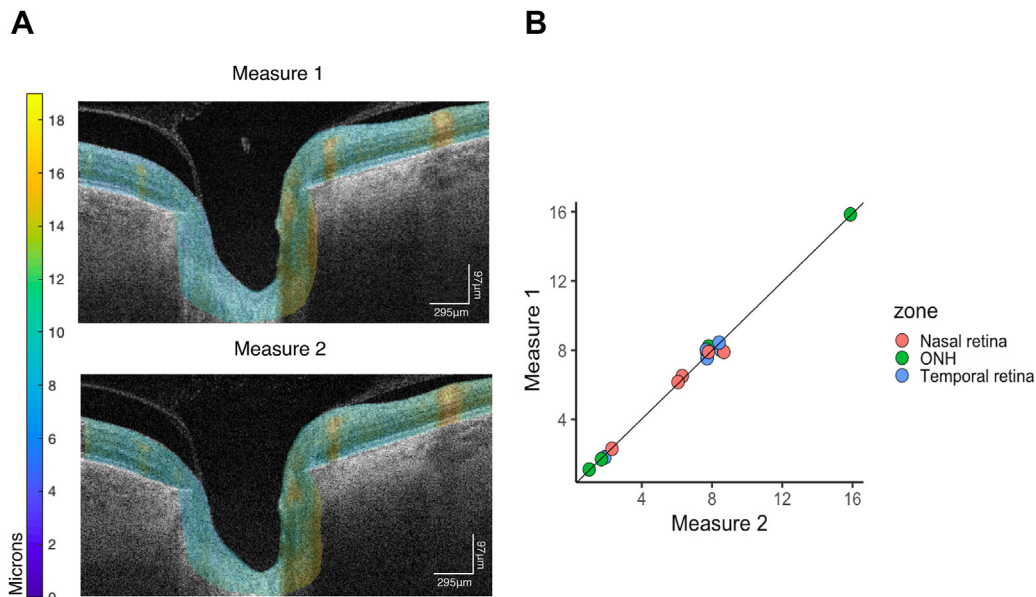

Figure 5. Test−retest algorithm validation. **A,** Pulsatile displacement maps calculated on different days for the same subjects. **B,** Five eyes of 5 different healthy individuals were measured at 2 different time points; pulsatile deformation was calculated in nasal and temporal retinas and optic nerve head (ONH). Two-way random-effects model resulted in an intraclass correlation coefficient of 0.99 (95% confidence interval, 0.965−0.995; $P \leq 0.005$).
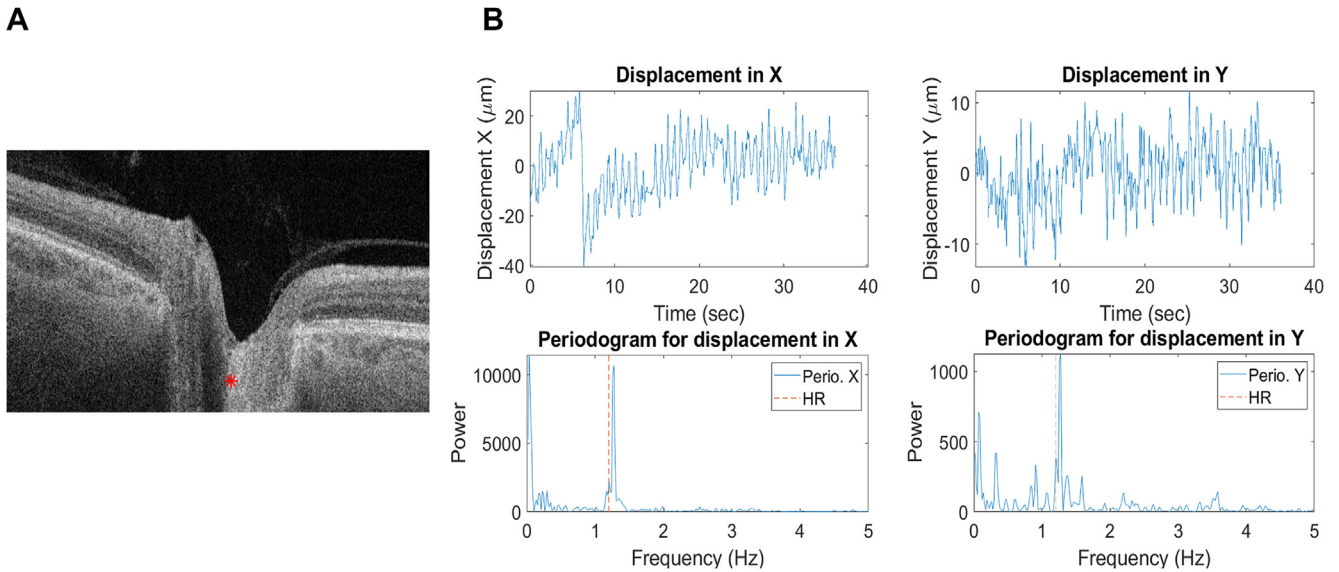
A

B

Figure 6. Tracking the trajectory of 1 pixel. An initial image location was determined (x_0, y_0) at the first frame (t_0); displacement fields were computed for all consecutive frames. **A,** Example of a pixel chosen on a typical B-scan. **B,** Top plots show the horizontal (left) and vertical (right) components of the trajectories. Bottom plots show Lombe−Scargle periodograms' corresponding frequency analysis displaying movement at the heart rate frequency for the x-axis (left) and y-axis (right). HR: heart rate.

displacement were calculated and compared in 3 areas: in the nasal and temporal retinas and in the ONH. One B-scan per video was manually segmented by the same observer by demarcating the ONH using an approximately 200-μm line extending from the Bruch's membrane opening to the retinal surface on both the nasal and temporal sides. Given the physiological relevance of the ONH in glaucoma, the analysis was centered on the segmented area shown in Figure 7B.

It is widely accepted that myopic eyes have altered biomechanical properties compared with eyes of normal AL.[36] Not only are there changes in the optic disc insertion, peripapillary atrophy, peripapillary scleral thickness, and scleral rigidity, but the LC also gets thinner with longer AL.[37–42] Therefore, our cohort was divided into 2 groups using an AL cut-off of 25 mm to compare the ONH deformation in both cohorts.

For the AL of < 25 mm group (n = 9), we observed that the median pulsatile displacement in the ONH was 7.8 ± 1.3 μm in the primary position and 8.9 ± 1.2 μm in abduction (Fig 7C, top). The Wilcoxon test showed a significant difference ($P \leq 0.005$) between the 2 paired measures. In the nasal retina, there was a median pulsatile deformation of 5.8 ± 0.9 μm in the primary position and 7.1 ± 1.3 μm for abduction ($P \leq 0.005$), whereas in the temporal retina there was a pulsatile deformation of 7.2 ± 1.3 μm and 7.8 ± 1.8 μm, respectively ($P \leq 0.3$). The most relevant area for the analysis—the ONH—showed a 12.2% increase in the median pulsatile deformation in abduction compared with the primary position, and an increase can be observed in all analyzed subjects when primary position and abduction are compared (Fig 7C, top). There was no correlation between IOP and median

ONH pulsatile deformation; however, the measured IOPs were all normal, ranging from 12 to 19 mmHg. No relevant association was found between age, sex, and median pulsatile deformation values in the multivariate analysis performed for these characteristics.

Notwithstanding the small sample size, the results for the myopic group (AL ≥ 25 mm, n = 5) do not display the same changes in pulsatile deformation in abduction and primary position that can be observed in the normal eye cohort. At the ONH, the median pulsatile deformation was 9.6 ± 1.5 μm in the primary position and 8.6 ± 1.2 μm in abduction ($P = 0.3$, Fig 7C, bottom). This trend was maintained at the nasal and temporal sections in which no significant difference was found when comparing both positions. In the nasal retina, there was a median pulsatile deformation of 6.7 ± 1.5 μm in the primary position and 7.1 ± 1.1 μm for abduction ($P = 0.8$), whereas in the temporal retina there was a pulsatile deformation of 7.7 ± 4.4 μm and 7.17 ± 4.2 μm, respectively ($P = 0.19$). Wilcoxon test was used to compare the populations. There was no association between age, sex, and median pulsatile deformation values for this cohort in the multivariate analysis performed for these characteristics. Additional analysis comparing the deformation in the x- and y-axes independently can be found in Supplemental Appendix 1.

We performed an analysis of the vascular retinal tissue based on ad hoc OCT angiography and the reduced noise video to identify vessels within the scan. Both the methods yielded equivalent results, that is, while excluding vascular pixels, the displacement in each of the considered regions analyzed decreased (as vascular areas are highly variable) but the comparisons for different cohorts remained identical (Supplemental Appendix 2 [available at
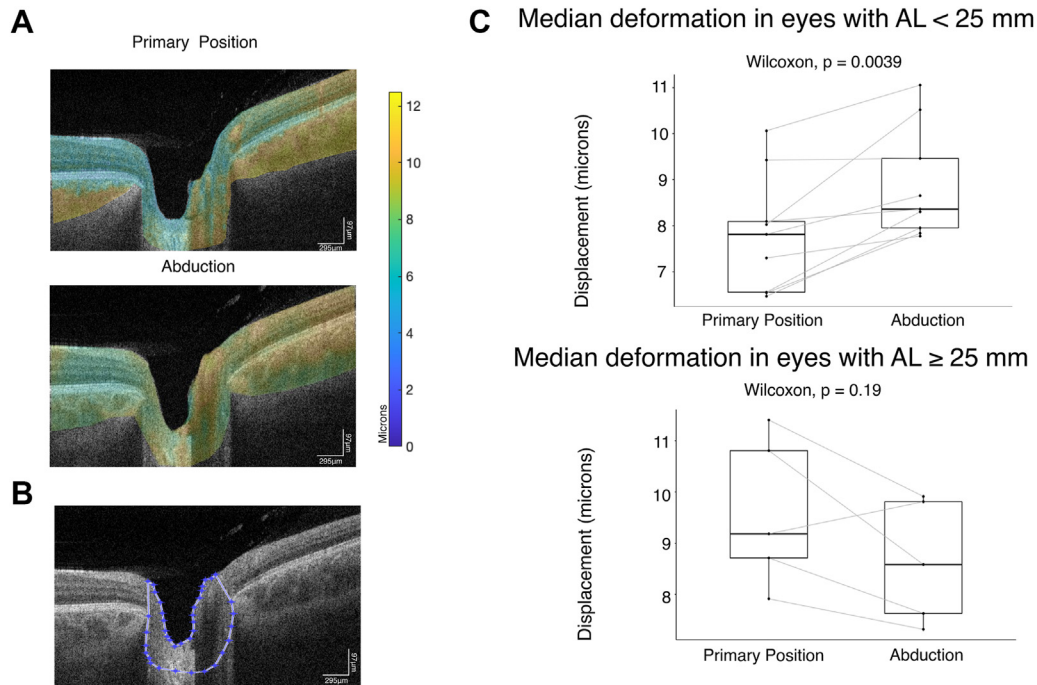
Figure 7. Optic nerve head (ONH) pulsatile displacement maps in different eye gazes. The tissue displacement of the optic nerve caused by horizontal eye movements induces a change in the pulsatile deformation of the ONH. **A,** Pulsatile displacement maps in primary position and abduction. **B,** The area considered for analysis of pulsatile changes. **C,** Median pulsatile displacement changes in primary position and abduction for 2 cohorts of different axial length (AL).

www.ophthalmologyscience.org] for these results and a more detailed description of the algorithms). Furthermore, upon analysis inside the vascular lumen areas, all differences disappeared.

Discussion

The integrity of the LC is vital to mitigate biomechanical insults to the ONH axons. Biomechanical models suggest that it is not a passive matrix affected by the IOP but is rather a dynamic structural part of the physiology of the ONH.[43] We developed a new approach to measure the dynamic properties of the ONH. To compensate for the lack of ground truth deformation, detailed numerical analyses were performed to benchmark our analysis pipeline. Our results demonstrate that the demons algorithm is able to detect pulsatile deformation in a video obtained using OCT.

Recent studies in primates[17] and mice[16] also used the concept of analyzing consecutive B-scans to measure deformation after artificially induced high IOP changes. They show bigger LC displacements with higher IOP. The use of anesthetized animal models allowed high-quality imaging to mitigate some of the noise that is common in nondilated volunteer patients.

Our method can detect a large range of amplitude of movement, beyond what was observed experimentally. The algorithm resists normal noise levels, as $\sigma^2 = 10^{-4}$ corresponds to an error of approximately 0.2 and 0.4 μm in Speckle and Gaussian distributions, and conservative values of variance such as $\sigma^2 = 10^{-2}$ correspond to approximately 1 and 1.5 μm absolute errors for the same distributions.

Noise could become relatively critical when displacement fields are small, as intensity changes might introduce artifacts in otherwise almost identical images; thus, we used a time lag $\Delta\tau$ of 10 frames for analysis, to capture larger displacements. Longer $\Delta\tau$ is in principle better, and half the cardiac cycle should be ideal; however, the eye-tracker pauses impose a severe limitation to extending $\Delta\tau$. A typical video has approximately 30 eye-tracker pauses, that is, producing an uninterrupted time series of roughly 100 frames. Considering that we avoid calculating $\vec{\mu}$ of 2 images with pauses in between, longer $\Delta\tau$ greatly reduces the number of pairs available for analysis. In our hands, $\Delta\tau$ of 10 frames (approximately 100 milliseconds) was a reasonable compromise.

A careful analysis of the performance of the registration approach on individual videos is necessary to discard measurements that cannot be adequately analyzed. Indeed, this strict limitation reduced the number of usable videos from an original cohort of 35 patients (70 videos), in that only 38 videos were included in the study. Excessive movement or blinking were the main factors creating difficulty in obtaining adequate registration, which were particularly noticeable in abduction. Thus, improvements in the analysis pipeline or imaging modalities are still critical to be able to exploit this technology in challenging cases.

At present, our analysis does not exclusively consider cardiac pulsations, as the detection of movement at the heart frequency is only used as quality control to verify the

validity of registration and computation of displacement fields. Thus, the deformation we currently measure does not filter out movements that are not driven by blood flow. We assume that most of the observed deformations are driven by pulsatile blood flow in the choroid or retina and the resultant pulsatility of the IOP. Future work combining our method with the exploration of the sources of distinct types of deformation would provide further insight into the biomechanics of the ONH.

We proved that our method is reproducible by calculating the correlation between 2 measures obtained on the same subject at different time points with a 2-way random-effects model.[44] We obtained a very high intraclass correlation, which suggests that the method could be translated to clinical applications. Nonetheless, the reproducibility was explored in a very small cohort of healthy subjects and should also be investigated in pathological scans and in different clinical scenarios. Numeric simulation shows that the demons algorithm is able to detect tissue deformation of various patterns and amplitudes. The performance decreases when noise is added, and this needs further investigation for clinical settings, in which good-quality images may be more challenging to obtain.

We observed changes in the pulsatile deformation of the ONH when the tissue displacement of the optic nerve changed in different eye gazes. Because of the hardware design, it was not possible to rotate the head and obtain a good-quality scan in adduction because of obstruction by the nose. However, even taking into account that abduction induces less strain than adduction,[33] the method was able to detect changes in the pulsatile deformation between the primary position and abduction. Furthermore, this change is absent in a cohort of myopic individuals. One reasonable explanation for larger displacement fields in abduction in the normal AL cohort is that vessels become constricted as the tension on the optic nerve increases, yielding larger pulsatile changes when blood flows.[45] Indeed, a similar behavior has been described in cardiovascular physiology.[46] The Korotkoff sounds, used to manually estimate the systemic blood pressure, are a product of a pulsatile wave that hits the arterial wall when the change in the vessel diameter affects the speed at which the blood circulates in the intravascular space.[46,47] Nonetheless, more research is required to support this mechanism in ophthalmic tissue, as this explanation remains speculative.

These conclusions were obtained from a very small cohort, thus limiting the possibility of extracting medically useful conclusions yet. Furthermore, we are aware that noise may yield an overestimation of the precise magnitude of tissue displacement. However, our controls and stringent separation of vascular and avascular pixels rendered consistent behavior between eye gazes and patient cohorts.

High-frequency swept-source OCT has opened the door to the observation of the dynamics of the human eye in vivo. The method we introduce aims to contribute to the current knowledge on ophthalmic biomechanics and to offer a noninvasive way to explore the pulsatile displacement of the ONH. These data could also be used to implement numerical methods to estimate local strain properties of the human ONH using standard equipment available in ophthalmology clinics.

Footnotes and Disclosures

Correspondence:
Santiago Costantino, PhD, 5415 Assumption Blvd, Montreal, Quebec H1T 2M4, Canada. E-mail: Santiago.costantino@umontreal.ca.

References

1. Strouthidis NG, Girard MJA. Altering the way the optic nerve head responds to intraocular pressure—a potential approach to glaucoma therapy. *Curr Opin Pharmacol*. 2013;13:83—89.
2. Levy NS, Crapps EE. Displacement of optic nerve head in response to short-term intraocular pressure elevation in human eyes. *Arch Ophthalmol*. 1984;102:782—786.
3. Zeimer RC, Ogura Y. The relation between glaucomatous damage and optic nerve head mechanical compliance. *Arch Ophthalmol*. 1989;107:1232—1234.
4. Yan DB, Coloma FM, Metheetrairut A, et al. Deformation of the lamina cribrosa by elevated intraocular pressure. *Br J Ophthalmol*. 1994;78:643—648.
5. Kirby MA, Pelivanov I, Song S, et al. Optical coherence elastography in ophthalmology. *J Biomed Opt*. 2017;22:1—28.
6. Shin A, Yoo L, Park J, Demer JL. Finite element biomechanics of optic nerve sheath traction in adduction. *J Biomech Eng*. 2017;139:101010.
7. Takusagawa HL, Hoguet A, Junk AK, et al. Swept-source OCT for evaluating the lamina cribrosa: a report by the American Academy of Ophthalmology. *Ophthalmology*. 2019;126:1315—1323.
8. Jin Y, Wang X, Irnadiastputri SFR, et al. Effect of changing heart rate on the ocular pulse and dynamic biomechanical behavior of the optic nerve head. *Invest Ophthalmol Vis Sci*. 2020;61:27.
9. Choi W, Park JH, Ha H, Lee SJ. Flow induced deformation of vulnerable stenosis under pulsatile flow condition. *Phys Rev Fluids*. 2020;5:043101.
10. Nagaoka R, Iwasaki R, Arakawa M, et al. Basic study of intrinsic elastography: relationship between tissue stiffness and propagation velocity of deformation induced by pulsatile flow. *Jpn J Appl Phys*. 2015;54:07HF08.
11. Daneshvar R, Nouri-Mahdavi K. Optical coherence tomography angiography: a new tool in glaucoma diagnostics and research. *J Ophthalmic Vis Res*. 2017;12:325—332.
12. Beaton L, Mazzaferri J, Lalonde F, et al. Non-invasive measurement of choroidal volume change and ocular rigidity through automated segmentation of high-speed OCT imaging. *Biomed Opt Express*. 2015;6:1694—1706.
13. Sayah DN, Mazzaferri J, Descovich D, et al. The association between ocular rigidity and neuroretinal damage in glaucoma. *Invest Ophthalmol Vis Sci*. 2020;61:11.
14. Hidalgo-Aguirre M, Costantino S, Lesk MR. Pilot study of the pulsatile neuro-peripapillary retinal deformation in glaucoma and its relationship with glaucoma risk factors. *Curr Eye Res*. 2017;42:1620—1627.
15. Labounkova I, Labounek R, Nestrasil I, et al. Blind source separation of retinal pulsatile patterns in optic nerve head video-recordings. *IEEE Trans Med Imaging*. 2021;40:852—864.
16. Baumann B, Merkle CW, Augustin M, et al. Pulsatile tissue deformation dynamics of the murine retina and choroid mapped by 4D optical coherence tomography. *Biomed Opt Express*. 2022;13:647—661.
17. Kim J, Gardiner SK, Ramazzotti A, et al. Strain by virtual extensometers and video-imaging optical coherence tomography as a repeatable metric for IOP-Induced optic nerve head deformations. *Exp Eye Res*. 2021;211:108724.
18. Cahill ND, Noble JA, Hawkes DJ. A demons algorithm for image registration with locally adaptive regularization. In: *Medical Image Computing and Computer-Assisted Intervention — MICCAI 2009*. Berlin Heidelberg: Springer; 2009:574—581.
19. Thirion JP. Image matching as a diffusion process: an analogy with Maxwell's demons. *Med Image Anal*. 1998;2:243—260.
20. Vercauteren T, Pennec X, Malis E, et al. Insight into efficient image registration techniques and the demons algorithm. *Inf Process Med Imaging*. 2007;20:495—506.
21. Vercauteren T, Pennec X, Perchant A, Ayache N. Non-parametric diffeomorphic image registration with the demons algorithm. *Med Image Comput Comput Assist Interv*. 2007;10:319—326.
22. Cachier P, Pennec X, Ayache N. *Fast no n rigid matching by gradient descent: study and improvements of the "demons" algorithm*. https://hal.inria.fr/inria-00072962/. Accessed August 9, 2021.
23. Guimond A, Roche A, Ayache N, Meunier J. Three-dimensional multimodal brain warping using the demons algorithm and adaptive intensity corrections. *IEEE Trans Med Imaging*. 2001;20:58—69.
24. Mattes D, Haynor DR, Vesselle H, et al. Nonrigid multimodality image registration. In: *Medical Imaging 2001: Image Processing*. Vol 4322. International Society for Optics and Photonics; 2001:1609—1620.
25. Registration — ANTsPy master documentation. Available at: https://antspy.readthedocs.io/en/latest/registration.html. Accessed February 7, 2022.
26. Suh MH, Zangwill LM, Manalastas PIC, et al. Optical coherence tomography angiography vessel density in glaucomatous eyes with focal lamina cribrosa defects. *Ophthalmology*. 2016;123:2309—2317.
27. Kashani AH, Chen CL, Gahm JK, et al. Optical coherence tomography angiography: a comprehensive review of current methods and clinical applications. *Prog Retin Eye Res*. 2017;60:66—100.
28. Dielemans I, Vingerling JR, Hofman A, et al. Reliability of intraocular pressure measurement with the Goldmann applanation tonometer in epidemiological studies. *Graefes Arch Clin Exp Ophthalmol*. 1994;232:141—144.
29. Niccolai M, Varanini M, Macerata A, et al. Analysis of non-stationary heart rate series by evolutionary periodogram. In: *Computers in Cardiology 1995*. New York: IEEE; 1995:449—452.
30. Li TH. Laplace periodogram for time series analysis. *J Am Stat Assoc*. 2008;103:757—768.
31. Suh SY, Le A, Shin A, et al. Progressive deformation of the optic nerve head and peripapillary structures by graded horizontal duction. *Invest Ophthalmol Vis Sci*. 2017;58:5015—5021.
32. Chang MY, Shin A, Park J, et al. Deformation of optic nerve head and peripapillary tissues by horizontal duction. *Am J Ophthalmol*. 2017;174:85—94.
33. Wang X, Beotra MR, Tun TA, et al. In vivo 3-dimensional strain mapping confirms large optic nerve head deformations following horizontal eye movements. *Invest Ophthalmol Vis Sci*. 2016;57:5825—5833.
34. Chang M, Shin A, Park J, et al. Optical coherence tomography (OCT) demonstrates deformation of optic cup and peripapillary tissues by horizontal duction. Meeting abstract. *Invest Ophthalmol Vis Sci*. 2016;57:10—6601.
35. Wang X, Rumpel H, Lim WEH, et al. Finite element analysis predicts large optic nerve head strains during horizontal eye movements. *Invest Ophthalmol Vis Sci*. 2016;57:2452—2462.

36. Curtin BJ, Karlin DB. Axial length measurements and fundus changes of the myopic eye. I. The posterior fundus. *Trans Am Ophthalmol Soc*. 1970;68:312−334.
37. Jonas JB, Ohno-Matsui K, Panda-Jonas S. Optic nerve head histopathology in high axial myopia. *J Glaucoma*. 2017;26: 187−193.
38. Yu AY, Shao H, Pan A, et al. Corneal biomechanical properties in myopic eyes evaluated via Scheimpflug imaging. *BMC Ophthalmol*. 2020;20:279.
39. Wu W, Dou R, Wang Y. Comparison of corneal biomechanics between low and high myopic eyes-a meta-analysis. *Am J Ophthalmol*. 2019;207:419−425.
40. Jonas JB, Kutscher JN, Panda-Jonas S, Hayreh SS. Lamina cribrosa thickness correlated with posterior scleral thickness and axial length in monkeys. *Acta Ophthalmol*. 2016;94: e693−e696.
41. Bell GR. Biomechanical considerations of high myopia: Part I–physiological characteristics. *J Am Optom Assoc*. 1993;64: 332−338.
42. Bell GR. Biomechanical considerations of high myopia: Part II–biomechanical forces affecting high myopia. *J Am Optom Assoc*. 1993;64:339−345.
43. Sigal IA, Flanagan JG, Tertinegg I, Ethier CR. Predicted extension, compression and shearing of optic nerve head tissues. *Exp Eye Res*. 2007;85:312−322.
44. Vardeman SB, VanValkenburg ES. Two-way random-effects analyses and gauge R&R studies. *Technometrics*. 1999;41: 202−211.
45. Chuangsuwanich T, Wang X, Tun TA, et al. Adduction induces abnormally large optic nerve head strains in normal tension glaucoma subjects. *Invest Ophthalmol Vis Sci*. 2020;61:1005−1005.
46. Levick JR. *An Introduction to Cardiovascular Physiology*. Oxford, United Kingdom: Butterworth-Heinemann; 2013.
47. Peretz A, Leotta DF, Sullivan JH, et al. Flow mediated dilation of the brachial artery: an investigation of methods requiring further standardization. *BMC Cardiovasc Disord*. 2007;7:11.